▌2D Materials
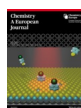
Defect Engineering of Two-Dimensional Molybdenum Disulfide

Xin Chen,[a] Peter Denninger,[b] Tanja Stimpel-Lindner,[c] Erdmann Spiecker,[b]
Georg S. Duesberg,[c] Claudia Backes,[d] Kathrin C. Knirsch,[a] and Andreas Hirsch*[a]

Abstract: Two-dimensional (2D) molybdenum disulfide (MoS$_2$) holds great promise in electronic and optoelectronic applications owing to its unique structure and intriguing properties. The intrinsic defects such as sulfur vacancies (SVs) of MoS$_2$ nanosheets are found to be detrimental to the device efficiency. To mitigate this problem, functionalization of 2D MoS$_2$ using thiols has emerged as one of the key strategies for engineering defects. Herein, we demonstrate an approach to controllably engineer the SVs of chemically exfoliated MoS$_2$ nanosheets using a series of substituted thiophenols in solution. The degree of functionalization can be tuned by varying the electron-withdrawing strength of substituents in thiophenols. We find that the intensity of 2LA(M) peak normalized to A$_{1g}$ peak strongly correlates to the degree of functionalization. Our results provide a spectroscopic indicator to monitor and quantify the defect engineering process. This method of MoS$_2$ defect functionalization in solution also benefits the further exploration of defect-free MoS$_2$ for a wide range of applications.

Introduction

Research on two-dimensional (2D) transition-metal dichalcogenides (TMDs) has boomed in the last decade due to their exceptional physical and chemical properties arising from ultrathin 2D structures.[1–4] As a prototype of 2D TMDs, the single layer molybdenum disulfide (MoS$_2$) exhibits a direct band gap (1.9 eV) combined with good carrier mobility (100 cm^{2}V^{-1}s^{-1}) and on/off ratio (10^8) in field effect transistors, as well as an excellent chemical stability, which makes it an appealing material for use in electronic and optoelectronic applications.[2,5–7] To date, a wide array of strategies has been developed to prepare single or few-layer MoS$_2$ nanosheets, including mechanical exfoliation (ME), chemical vapor deposition (CVD), liquid-phase exfoliation (LPE), chemical (CE) and electro-chemical (ECE) exfoliation, and wet-chemical synthesis.[8–15] Among them, solution-based exfoliation techniques such as LPE, CE and ECE hold great promise in terms of low-cost, scalability and convenience for multicomponent hybridization. However, the exfoliation procedures would inevitably introduce additional defects to the MoS$_2$ lattice.[16–20] For example, sulfur vacancies (SVs) have been widely observed in exfoliated MoS$_2$ nanosheets using high resolution microscopy.[18,21] These SVs act as trap states or scattering sites, affecting the charge carrier mobility and photoluminescence quantum yield (QY), thus are considered to be detrimental for the efficiency of electronic and optoelectronic devices. On the flip side, the unsaturated Mo sites at SVs are more reactive compared to the dangling-bond free basal plane, which avails to tailor the properties of 2D MoS$_2$ through the chemical modification. Therefore, defect engineering of 2D MoS$_2$ via either fixing or functionalizing the SVs has emerged as a key strategy to modulate the physical and chemical properties of MoS$_2$-based materials.[5,22–25]

Inspired by the high affinities of thiol moieties to the SVs of MoS$_2$, a variety of organic thiols (e.g. alkyl thiols and thiophenols, etc.) has been applied to functionalize defective MoS$_2$ nanosheets. It is widely acknowledged that the thiol group (-SH) can bind to unsaturated Mo in SVs, leading to either repaired (chemisorption of thiol molecules at SVs followed by

[a] Dr. X. Chen, Dr. K. C. Knirsch, Prof. A. Hirsch
Department of Chemistry and Pharmacy
Friedrich–Alexander-Universität (FAU) Erlangen-Nürnberg
Nikolaus-Fiebiger-Straße 10, 91058 Erlangen (Germany)
E-mail: andreas.hirsch@fau.de

[b] P. Denninger, Prof. E. Spiecker
Center for Nanoanalysis and Electron Microscopy (CENEM) & Institute of
Micro- and Nanostructure Research (IMN)
Interdisciplinary Center for Nanostructured Films (IZNF)
Friedrich–Alexander-Universität (FAU) Erlangen-Nürnberg
Cauerstraße 3, 91058 Erlangen (Germany)

[c] Dr. T. Stimpel-Lindner, Prof. G. S. Duesberg
Institute of Physics, EIT 2, Faculty of Electrical Engineering and Information
Technology
Universität der Bundeswehr
85579 Neubiberg (Germany)

[d] Dr. C. Backes
Institute of Physical Chemistry
Heidelberg University
Im Neuenheimer Feld 253, 69120 Heidelberg (Germany)

Chemistry–A European Journal

Full Paper
doi.org/10.1002/chem.202000286

Chemistry Europe
European Chemical
Societies Publishing

cleavage of S—C bonds) or functionalized (chemisorption of thiol molecules at SVs) MoS$_2$ nanosheets.[24,26–28] Yet a recent experimental study showed another possibility: during the functionalization process, it was found that thiol monomers were readily oxidized to corresponding disulfides, which physisorbed on the surface of MoS$_2$ instead of filling in SVs.[29,30] Later on, another theoretical investigation argued that the dimerization process is thermodynamically possible when S adatoms are present. Nevertheless, in the presence of SVs, the formed disulfide would be reduced back to thiols immediately and proceeded eventually as the SVs-repairing process.[31] The discrepancy in the previous experimental studies and theoretical simulations is likely attributed to the difference in size and defect density of the MoS$_2$ samples, and the applied reaction conditions. For example, the presence of O$_2$ in the reaction medium may expedite the oxidation of thiols[30] and MoS$_2$ through gradual substitution of surface sulfur with oxygen to form oxidized SVs over the lattice.[32–34] The disputable mechanisms of MoS$_2$/thiol interaction bring about the complexity of the possible reaction products as well as the challenges to precisely tailor the MoS$_2$ properties using thiols.
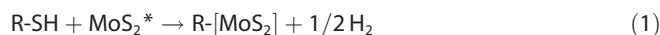
In addition, the reactions between thiols and defective MoS$_2$ are expected to be very sensitive to the electronic effects of the functional groups in thiols.[28,35] For example, the theoretical simulation pointed out that thiols with electron-donating groups (EDG) tend to accelerate the SVs-repairing process, while thiols with electron-withdrawing groups (EWG) favor the functionalization process.[36] The kinetic study of the oxidation of thiols to disulfides in the presence of MoS$_2$ showed that the reaction rate decreased with increasing the pK_a of the thiols.[30] However, no systematic experimental research on SVs-engineered MoS$_2$ nanosheets using both EDG- and EWG-functionalized thiols has been carried out to date. Such a study would allow for a comprehensive understanding of the thiol-chemistry based defect engineering process.

Here, we demonstrate a facile strategy to controllably functionalize chemically exfoliated MoS$_2$ nanosheets using thiophenol derivatives. The external stimuli such as temperature and O$_2$ level were strictly controlled to avoid the suspicious disulfide generation and suppress other side reactions such as oxidation of SVs. The modified MoS$_2$ was characterized by thermogravimetric analysis coupled with mass spectrometry (TGA-MS), Fourier-transform infrared spectroscopy (FT-IR), X-ray photoelectron spectroscopy (XPS), transmission electron microscopy (TEM), atomic force microscopy (AFM), Raman spectroscopy, and UV/Vis spectroscopy. A series of substituted thiophenols was implemented in this study to investigate the influence of substituents (EWG or EDG) on the reactivity of thiophenols with 2D MoS$_2$ and the effect of different surface addends on the thermal stability and optical properties of MoS$_2$ nanosheets. A correlation between the degree of functionalization and the Hammett parameter of *para*-substituted phenyls was extracted. A spectroscopic signature associated with the defect density of MoS$_2$ nanosheets was proposed based on the Raman analysis. Our results provide a practical guide to modify the MoS$_2$ surface using thiols in a controllable way and set a

basis for the precise exploration of the defect-engineered MoS$_2$.

Results and Discussion

By summarizing the reported theoretical predictions and experimental observations, we noted that three reactions may take place coincidentally or separately when reacting defective MoS$_2$ nanosheets with organic thiols as detailed below [Eqs. (1), (2), (3)]:

$$R\text{-}SH + MoS_2^* \rightarrow R\text{-}[MoS_2] + 1/2\,H_2 \tag{1}$$

$$R\text{-}SH + MoS_2^* \rightarrow MoS_2 + RH \tag{2}$$

$$R\text{-}SH + MoS_2^* \rightarrow MoS_2^* + 1/2\,RSSR + 1/2\,H_2 \tag{3}$$

in which MoS$_2$* denotes the defective MoS$_2$ slab with mono sulfur vacancy.

(1) Functionalization process, in which reactive sulfur-containing fragments (e.g. thiolates or thiyl radicals) bind to the exposed, unsaturated Mo atoms at SVs of MoS$_2$ (MoS$_2$*), leading to the formation of covalently functionalized MoS$_2$ (R-[MoS$_2$]) likely under H$_2$ generation.[24,37] (2) SV repairing process, in which chemisorption of thiols at SVs of MoS$_2$ is accompanied/followed by the cleavage of S—C bonds, resulting in the quasi-perfect MoS$_2$ ([MoS$_2$]) with repaired SVs. Hydrocarbon byproducts are possibly formed during this process.[38,39] (3) Dimerization process, in which MoS$_2$ catalyzes the oxidation of thiols to disulfides with little change to itself.[29,31] Accordingly, the species adsorbed on the MoS$_2$ surface can be categorized into two classes depending on their interaction type with MoS$_2$: Class I. Disulfides (RSSR) and hydrocarbon byproducts (RH), which are physisorbed on the surface; Class II. Covalently bonded thiol moieties (RS-), which are chemically bound to Mo atoms at SVs.

To controllably engineer the SVs of MoS$_2$ nanosheets, we set out to limit the generation of physisorbed species and increase the possibility for chemisorption of thiols at SVs. To this end, we performed the functionalization reaction by controlling the following parameters. (1) O$_2$ level: All the reactions were performed under argon (Ar) atmosphere. (2) Defects of MoS$_2$: MoS$_2$ nanosheets were prepared by chemical exfoliation (*ce*-MoS$_2$), which involves the lithium intercalation of bulk MoS$_2$ followed by sonication of intercalated compounds in water under Ar. The harsh reaction conditions allow for the production of defective MoS$_2$ flakes with relatively small sizes. Moreover, monolayers and bilayers are predominantly produced, offering rich binding sites at edges and SVs in *ce*-MoS$_2$ for thiols. Thus, a high degree of covalent functionalization and a significant change of the surface properties is anticipated after SVs engineering, which facilitates characterization. (3) Temperature: All the reactions were carried out under mild conditions (50 °C) instead of high local temperatures (e.g. through ultrasonication) in contrast to previous procedures.[24,29] Previous theoretical studies have indicated that both functionalization [Eq. (1)] and repairing processes [Eq. (2)] are exothermic with very low

Chemistry–A European Journal

Full Paper
doi.org/10.1002/chem.202000286

**Chemistry
Europe**
European Chemical
Societies Publishing

activation barriers while the dimerization process [Eq. (3)] is endothermic and requires relatively high activation energy.[31] Thus, avoiding high local temperatures during the reaction can potentially limit the formation of disulfides.

Preparation of chemically exfoliated and defect-engineered MoS$_2$ nanosheets

MoS$_2$ nanosheets were prepared by the chemical exfoliation method following the procedure developed by Morrison[11] et al. with some modifications (see the supporting information for details). Briefly, bulk MoS$_2$ powder (300 mg) was dispersed in an excess amount of n-butyllithium (3.0 mL, 2.0 M in cyclohexane) and vigorously stirred at room temperature in a glovebox for two days. The resulting mixture was diluted with hexane and then added dropwise to de-ionized water at 0 °C, which was accompanied by a conspicuous hydrogen evolution. After the gas generation ceased, the organic impurities were removed by extraction with cyclohexane, and the aqueous phase was collected and deaerated by Ar flow for 15 min. The aqueous black slurry was then sonicated in a sonic bath under Ar protection for 1 h. The resulting dispersion was subjected to low-speed centrifugation to remove non-exfoliated MoS$_2$. The exfoliated material in the supernatant was collected and washed with de-ionized water through several times of high-speed centrifugation where very small sheets and LiOH were removed in the supernatant. The sediment after the washing steps was re-dispersed in de-ionized water for further functionalization and characterization.

Defect-engineered MoS$_2$ nanosheets were prepared by reacting freshly prepared chemically exfoliated MoS$_2$ with a series of thiophenols under inert atmosphere (Figure 1). Specifically, the aqueous dispersion of exfoliated MoS$_2$ nanosheets was mixed with 20 molar excess of the respective thiophenol dispersed in isopropanol. The mixture was subjected to the deaeration based on freeze-pump-thaw cycling for three times. Then the pre-treated solution was vigorously stirred at 50 °C for 48 h under Ar atmosphere. The resulting product was purified through washing with ethanol, isopropanol and water, and re-dispersed in de-ionized water or isopropanol for further characterization. Throughout this work, we refer the MoS$_2$ samples functionalized with 4-aminothiophenol, 4-methoxythio-

phenol, 4-isopropylthiophenol, thiophenol, 4-bromothiophenol, 4-mercaptobenzoic acid and 4-nitrothiophenol as NH$_2$Ph-MoS$_2$, OMePh-MoS$_2$, ProPh-MoS$_2$, Ph-MoS$_2$, BrPh-MoS$_2$, COOHPh-MoS$_2$, and NO$_2$Ph-MoS$_2$, respectively.

Characterization of chemically exfoliated and defect-engineered MoS$_2$ nanosheets

The AFM measurements (Figure 2a, 2b, and height profiles in S1) showed that the as-prepared ce-MoS$_2$ nanosheets are about 1.5–3 nm thick with rather rough surface profiles characteristic for ce-MoS$_2$.[40,41] The typical shape of 2D nanosheets is discerned with minimal aggregation. The lateral sizes range from 200–300 nm. In contrast, the AFM image of Ph-MoS$_2$, as a representative functionalized material, showed objects with a thickness of up to 8–10 nm. In many cases, the material lost the characteristic 2D shape, which is attributed to aggregation and random restacking in dispersion before deposition so that the nanosheets do not lie flat on the surface. However, even objects that show the characteristic shape of 2D nanosheets are 4–8 nm thick, possibly due to the chemical modification of the basal plane.
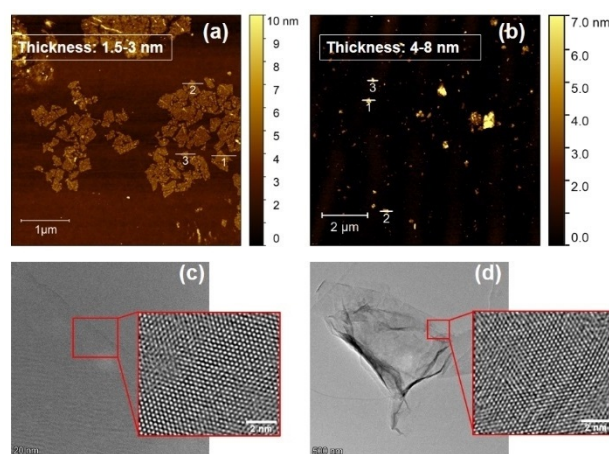

Figure 2. AFM images of ce-MoS$_2$ (a) and Ph-MoS$_2$ (b). High resolution TEM images of ce-MoS$_2$ (c) and Ph-MoS$_2$ (d).

The zeta potential (ζ) of a diluted aqueous dispersion of ce-MoS$_2$ was determined to be −52 mV, which is in accordance with the literature reported value,[42] validating the chemically exfoliated MoS$_2$ nanosheets are negatively charged. In comparison, the zeta potentials of NH$_2$Ph-MoS$_2$, OMePh-MoS$_2$, ProPh-MoS$_2$, Ph-MoS$_2$, BrPh-MoS$_2$, COOHPh-MoS$_2$, and NO$_2$Ph-MoS$_2$ were shifted to −32, −40, −35, −31, −35, −23 and −37 mV, respectively (Table 1). The positive shift of zeta potentials in MoS$_2$ samples after chemical modification demonstrates that the negative charge of ce-MoS$_2$ was partially removed after reaction with the thiophenols. It is noted that the colloidal stability of chemically modified materials such as NH$_2$Ph-MoS$_2$, ProPh-MoS$_2$, Ph-MoS$_2$, and BrPh-MoS$_2$ in water is decreased compared to ce-MoS$_2$, with the sedimentation of a dark-grey precipitate being discernible after a few hours. This is in agree-
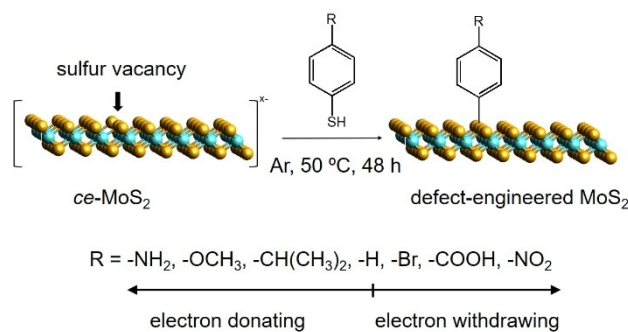

Figure 1. Schematic illustration showing the preparation of defect-engineered MoS$_2$ using substituted thiophenols.

Chemistry–A European Journal

Full Paper
doi.org/10.1002/chem.202000286

Chemistry Europe
European Chemical
Societies Publishing

Table 1. Key characteristics of ce-MoS$_2$ and defect-engineered MoS$_2$.

	Hammett Parameter	Zeta potential [mV]	Mass loss [%] (TGA)	L:MoS$_2$[a] (molar ratio)
ce-MoS$_2$	–	−45	5	–
NH$_2$Ph-MoS$_2$	−0.66	−32	1	0.011
OMePh-MoS$_2$	−0.27	−40	12	0.202
ProPh-MoS$_2$	−0.15	−35	4	0.056
Ph-MoS$_2$	–	−31	10	0.228
BrPh-MoS$_2$	0.23	−35	9	0.101
COOHPh-MoS$_2$	0.45	−23	26	0.480
NO$_2$Ph-MoS$_2$	0.78	−37	40	0.860

[a] The molar ratios are probably overestimated in NO$_2$Ph-MoS$_2$ and COOHPh-MoS$_2$, because the detachment of functional groups and decomposition of MoS$_2$ jointly contributed to the mass loss in the TGA.

ment with the presence of aggregated nanosheets in AFM, as well as the reduced magnitude of the zeta potential.

The morphology of both ce-MoS$_2$ and Ph-MoS$_2$ was also investigated by TEM. The TEM image of ce-MoS$_2$ (Figure 2c) showed the typical hexagonal lattice, which is consistent with previous literature.[43,44] Similar lattice features were also observed in the TEM image of Ph-MoS$_2$ (Figure 2d), demonstrating that the structure was preserved after thiophenol modification.

To quantify the nature and the amount of functionalities in the modified MoS$_2$ samples, we performed TGA-MS measurements as shown in Figure 3 and Figure S2. The TGA-MS profile of ce-MoS$_2$ showed a total mass loss of around 5% over the temperature range of 200–700 °C (Figure 3a), which was primarily due to the degradation of MoS$_2$. In comparison, Ph-MoS$_2$ displayed a two-step degradation with a significant total weight loss of approximately 10% at 550 °C. The major gaseous products evolved from the thermolysis of Ph-MoS$_2$ were identified as phenyl group related fragments ($m/z = 78, 77$, and 39, Figure 3b) with the maximum gas evolution rate at 408 °C, which were presumably derived from the detachment of chemisorbed phenyl addends.

Similarly, the mass loss between 300–550 °C was found to be 1%, 12%, 4%, 9%, 26%, and 40% for NH$_2$Ph-MoS$_2$, OMePh-MoS$_2$, ProPh-MoS$_2$, BrPh-MoS$_2$, COOHPh-MoS$_2$, and NO$_2$Ph-MoS$_2$, respectively. (Table 1) The characteristic mass peaks associated with the fragments of the phenyl group were also de-

tected in all the thiophenol derivatives modified MoS$_2$ samples (Figure S2). Besides this, some samples showed distinct mass signals related to substituted phenyl groups. For example, a peak at $m/z = 105$, which is corresponding to the C$_8$H$_9$ fragment of the isopropyl phenyl group (after cleavage of a methyl group), was detected in ProPh-MoS$_2$; and a peak at $m/z = 60$, which is corresponding to the C$_2$H$_4$O$_2$ (CH$_3$COOH) fragment, was detected in COOHPh-MoS$_2$.

To further decode the bonding nature between surface functionalities and MoS$_2$, a control experiment was carried out by mixing of ce-MoS$_2$ with toluene, which bears the phenyl ring but without the functional thiol tail (−SH), under the same reaction conditions and purified by following the same protocol as used for the functionalization of MoS$_2$. The TGA-MS profile of toluene treated ce-MoS$_2$ (Tol/MoS$_2$) exhibits a one-step degradation in the temperature range of 150–500 °C with the overall mass loss of 10% at 500 °C (Figure S3). The major fragment with $m/z = 64$ was detected at the maximum gas evolution rate of 272 °C, which was attributed to the generation of SO$_2$ by the degradation of MoS$_2$. The fragments with $m/z = 78, 77$, 15 (CH$_3$) were also identified, however in much lower quantities, that is, with reduced ion currents compared to SO$_2$, suggesting that the major amount of toluene has been removed during the purification step and the leftover traces that physisorbed on MoS$_2$ surface can be easily burned up at 200–300 °C. The distinct thermolysis behaviors of thiophenol modified MoS$_2$ samples compared to this Tol/MoS$_2$ manifest that functionalities are very likely chemically anchored onto MoS$_2$ nanosheets in the thiophenol modified MoS$_2$ samples.

Additionally, it is noted that the ion current of SO$_2$ ($m/z = 64$) derived from degradation of MoS$_2$ was constantly observed as the major product during the thermolysis of ce-MoS$_2$ (Figure 3a). In comparison, only a small trace of SO$_2$ was detected during the thermolysis of OMePh-MoS$_2$, ProPh-MoS$_2$, Ph-MoS$_2$, and BrPh-MoS$_2$, implying that modified MoS$_2$ displays better thermal stability compared to its non-modified parent and toluene-MoS$_2$ mixture. This is possibly attributed to the more robust structures of functionalized MoS$_2$, in which SVs were fixed by thiophenols. Interestingly, COOHPh-MoS$_2$ and NO$_2$Ph-MoS$_2$ are two exceptions, which showed detachment of surface functionalities accompanied by degradation of MoS$_2$. As the degree of functionalization for each defect-engineered sample was estimated based on the mass loss in TGA, we noticed that among all the samples, COOHPh-MoS$_2$ and NO$_2$Ph-MoS$_2$ showed significantly higher mass loss than the other derivative samples, thus implying a high degree of functionalization (see Table 1 for details). We suspect that the higher degree of functionalization in COOHPh-MoS$_2$ and NO$_2$Ph-MoS$_2$ induces local strains in the MoS$_2$ basal plane, which weakens the intralayer bonding of MoS$_2$ and thus makes these two samples less tolerant towards heating compared to other mildly modified MoS$_2$ samples (degree of functionalization ≤ 12% mass loss). We note that due to the observed decomposition in COOHPh-MoS$_2$ and NO$_2$Ph-MoS$_2$, the degree of functionalization from TGA-MS is likely overestimated slightly.

To gain more insight into the chemical composition and bonding state of Mo and S atoms in MoS$_2$ before and after
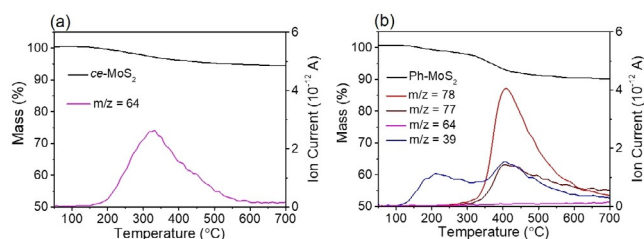
Figure 3. TGA-MS profiles of ce-MoS$_2$ (a) and Ph-MoS$_2$ (b). The major ion current in ce-MoS$_2$ is assigned to SO$_2$ ($m/z = 64$) derived from decomposing of MoS$_2$. The major ion currents in Ph-MoS$_2$ are the fragments C$_3$H$_3$$^+$ ($m/z = 39$), C$_6$H$_5$$^+$ ($m/z = 77$) and C$_6$H$_6$ ($m/z = 78$) associated with the detached and decomposed phenyl group.

modification with thiophenol, we investigated *ce*-MoS$_2$ and Ph-MoS$_2$ using XPS. The survey spectra (Figure S4 a) demonstrated a substantially increased content of carbon in Ph-MoS$_2$ compared to that in bare *ce*-MoS$_2$, which was likely due to the attachment of carbon-rich functionalities, phenyl moieties in this case. A close comparison of C 1s core level spectra (Figure S4 b) of bare *ce*-MoS$_2$ and Ph-MoS$_2$ revealed a distinct carbon species at 288.6 eV in Ph-MoS$_2$, which was presumably derived from the S–C components of attached thiophenol.

The Mo 3d core level spectra (Figure 4, left) of both *ce*-MoS$_2$ and Ph-MoS$_2$ displayed two dominant peaks and a small shoulder at higher binding energy, which can be fitted with four sets of doublet associated with Mo 3d$_{3/2}$ and Mo 3d$_{5/2}$ of 2H-MoS$_2$ (green), 1T-MoS$_2$ (blue), MoO$_3$ (purple), and MoO$_2$ (red). The presence of 1T-phase in *ce*-MoS$_2$ and Ph-MoS$_2$ demonstrates that the 1T-phase was partially preserved after defect engineering. We note that our previous investigations have proved that freshly prepared *ce*-MoS$_2$ contains over 70% of 1T-phase in contrast to the large content of 2H-phase in *ce*-MoS$_2$ (see Table S1 for the 1T/2H ratios in *ce*-MoS$_2$ and Ph-MoS$_2$).[40] We attribute this discrepancy to aging effects during the sample shipping and storage that are known to result in a conversion of the metastable 1T polytype to the 2H polytype.[40] In comparison, the phase transformation from 1T to 2H was decelerated in the defect-engineered sample, which is indicated by a larger relative portion of the 1T-phase in Ph-MoS$_2$. Most interestingly, the Mo 3d core level spectrum of Ph-MoS$_2$ shifted slightly towards the lower binding energy compared to that of *ce*-MoS$_2$, which is indicative of a mild rise of electron density around Mo in Ph-MoS$_2$. Similar shifts in XPS spectra have been demonstrated in n-doped MoS$_2$ systems.[35] We note that modifying *ce*-MoS$_2$ using thiophenol-based Lewis bases is expected to induce n-doping of the MoS$_2$ matrix.

The S 2p core level spectrum of *ce*-MoS$_2$ (Figure 4, right) was fitted into three sets of doublets: the predominant doublet at 163.4 and 162.3 eV is assigned to the S 2p$_{1/2}$ and S 2p$_{3/2}$ of
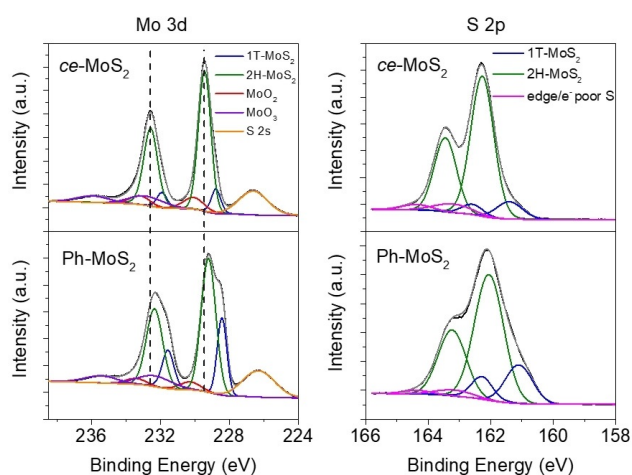
MoS$_2$; the doublet at higher binding energy to edges or electron-poor S species and the doublet at lower binding energy to electron-rich S species of the 1T polytype arising from the chemical exfoliation process. The S 2p core level spectrum of Ph-MoS$_2$ can also be fitted with three types of S components in analogy to bare *ce*-MoS$_2$. Compared to *ce*-MoS$_2$, the relative intensity of the electron-poor S species decreased slightly in Ph-MoS$_2$, which could be a manifestation of the chemical modification with thiophenol. However, we note that there are rather large degrees of freedom in fitting the S 2p core level spectra. Most importantly, the signals originating from free thiophenol and disulfide (normally at 164 and 165 eV)[28, 29] were not detected in Ph-MoS$_2$, indicating that no physisorbed thiophenol monomers or dimers are present. ^{1}H NMR (400 MHz, CD$_3$OD) spectrum of Ph-MoS$_2$ (Figure S5) further verified the absence of free thiophenol or disulfide in the Ph-MoS$_2$ sample after purification.

Collectively, the TGA-MS and XPS analysis demonstrated the presence of functional groups in Ph-MoS$_2$. The XPS and NMR experiments confirmed the absence of free thiophenol and corresponding dimers in Ph-MoS$_2$. Importantly, these functional groups did not change the bonding state of S atoms, instead, they affected the bonding environment of Mo atoms. These results verify the successful modification of MoS$_2$ nanosheets with thiophenol and the functional groups were likely bonded to the unsaturated Mo atoms at SVs instead of the surface S atoms.

We also characterized the thiophenol derivatives modified MoS$_2$ samples using FT-IR (Figure 5 a). The spectrum of NO$_2$Ph-MoS$_2$ (black curve in Figure 5 a) showed features at 1502 and 1334 cm^{-1}, corresponding to the asymmetric and symmetric stretches of the NO$_2$ group, and two characteristic peaks at 1593 and 1571 cm^{-1} arising from ν(C=C) stretching of the phenyl ring. The spectrum of COOHPh-MoS$_2$ (red curve in Figure 5 a) displayed intense peaks at 1677 and 1589 cm^{-1}, corre-
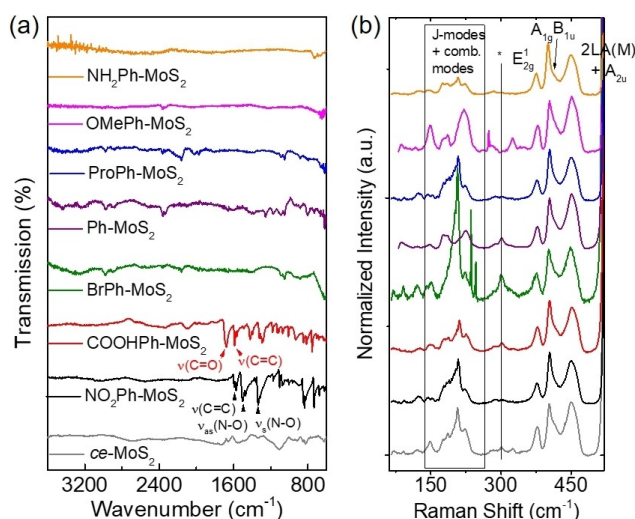
Figure 4. XPS core level spectra of Mo 3d and S 2p for *ce*-MoS$_2$ (top) and Ph-MoS$_2$ (bottom). The core level spectra show the presence of both 1T and 2H polytype of MoS$_2$ in both *ce*-MoS$_2$ and Ph-MoS$_2$. The 1T content is smaller than expected which we attribute to aging effects.

Figure 5. FT-IR spectra (a) and Raman spectra (b) of *ce*-MoS$_2$ and defect-engineered MoS$_2$. Color code: grey, *ce*-MoS$_2$; black, NO$_2$Ph-MoS$_2$; red, COOHPh-MoS$_2$; green, BrPh-MoS$_2$; purple, Ph-MoS$_2$; blue, ProPh-MoS$_2$; magenta, OMePh-MoS$_2$; and orange, NH$_2$Ph-MoS$_2$.

Chemistry–A European Journal

Full Paper
doi.org/10.1002/chem.202000286

Chemistry Europe
European Chemical
Societies Publishing

sponding to ν(C=O) and ν(C=C) stretching of the carboxyl phenyl moiety. Importantly, the feature correlated to ν(S–H) stretching at 2560 cm^{-1} in thiophenols was absent in COOHPh-MoS$_2$ and NO$_2$Ph-MoS$_2$. These results further verified the presence of substituted phenyl functionalities in NO$_2$Ph-MoS$_2$ and COOHPh-MoS$_2$, and the functionalities were presumably tethered on MoS$_2$ by the interaction between the thiol group and MoS$_2$. For the other five thiophenol derivatives modified MoS$_2$ samples, there were no discernible features associated with functionalities identified in the IR spectra, though TGA-MS analysis confirmed the successful coupling of substituted phenyl moieties with MoS$_2$. It is possibly due to the lower degree of functionalization in these mildly modified samples.

To investigate how our chemical modification affects the optical properties of MoS$_2$ nanosheets, we characterized *ce*-MoS$_2$ and thiophenols modified MoS$_2$ using Raman spectroscopy. Under resonant excitation ($\lambda = 633$ nm, Figure 5b), the Raman spectrum of *ce*-MoS$_2$ (grey curve) exhibits the typical in-plane vibrational mode, E$^1_{2g}$ at 377 cm^{-1}, and out-of-plane vibrational mode, A$_{1g}$ at 404 cm^{-1},[45] as well as the intense features at 150 to 330 cm^{-1}, which can be assigned to the superlattice 1T-phase related J-modes,[46,47] and the second order Raman mode, 2LA(M) at 450 cm^{-1} corresponding to the LA phonons at the M point in the Brillouin zone,[48] which is enhanced compared to excitation at higher energy. The resonant Raman spectra of thiophenols modified MoS$_2$ maintained almost all the above-mentioned features, verifying that the defect engineering process did not convert the crystal structure of MoS$_2$. In particular, the preserved features in the low frequency region indicated the presence of the 1T-phase in the functionalized MoS$_2$, which is in good agreement with our XPS results. We note that in some samples (e.g. BrPh-MoS$_2$, Ph-MoS$_2$, and OMePh-MoS$_2$), the features in this spectral region show a fingerprint distinct to *ce*-MoS$_2$. At the current stage, these features cannot be assigned and will therefore not be discussed further.

Tuning the degree of functionalization

To further elucidate the electronic influence of substituents in thiophenol derivatives on the reactivity with *ce*-MoS$_2$, we investigated the degree of functionalization as a function of the Hammett parameter of *para*-substituted phenyl (Figure 6 and Table S1). The Hammett parameter describes the electron-donating or -withdrawing effect of substituents on the phenyl ring. Basically, the more negative the Hammett parameter is, the stronger the electron-donating effect to the phenyl ring compared to hydrogen as a substituent. In turn, a positive Hammett parameter quantifies the electron-withdrawing effect. According to TGA-MS, the ratio of functional groups (denoted as L) per MoS$_2$ (molar L:MoS$_2$, atomic%) was calculated to be 1 at%, 20 at%, 6 at%, 23 at%, 10 at%, 48 at%, and 86 at% for NH$_2$Ph-MoS$_2$, OMePh-MoS$_2$, ProPh-MoS$_2$, Ph-MoS$_2$, BrPh-MoS$_2$, COOHPh-MoS$_2$, and NO$_2$Ph-MoS$_2$, respectively. For the samples BrPh-MoS$_2$, COOHPh-MoS$_2$, and NO$_2$Ph-MoS$_2$, the degree of functionalization might be overestimated, since the detachment of functional groups and decomposition of MoS$_2$
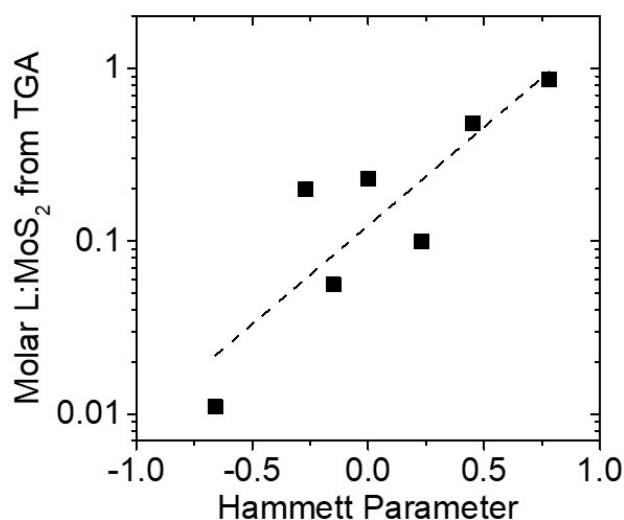
Figure 6. Plot of the degree of functionalization (ligand per MoS$_2$) as a function of the Hammett parameter.

jointly contributed to the mass loss in TGA. Overall, as illustrated in Figure 6, the degree of functionalization increases with increasing the Hammett parameter. This suggests that the electron poorer the thiophenols used, the more efficient the defect functionalization of the (negatively charged) *ce*-MoS$_2$.

Evolution of Raman spectra upon defect engineering

Considering that the assignment of the Raman modes < 300 cm^{-1} remains ambiguous in the 2H/1T co-existent and functionalized MoS$_2$ system, we focus on the analysis of the three main Raman modes here: E$^1_{2g}$, A$_{1g}$, and 2LA(M). Previous literature has shown that acoustic-phonon Raman scattering is sensitive to crystal defects (addends or vacancies) or disorders.[49,50] Therefore, we plot the intensity of the 2LA(M) peak normalized to the A$_{1g}$ peak (I$_{450}$/I$_{404}$) as a function of the degree of functionalization (Figure 7a). With increasing the degree of functionalization (decrease of defect density), I$_{450}$/I$_{404}$ first increases until reaching a maximum when L:MoS$_2 \approx 0.2$, and then decreases approaching to the value of the non-modified sample (*ce*-MoS$_2$).

To explain this phenomenon, we need to understand the influence of functionalization on the MoS$_2$ structure. As we noticed in the TGA-MS measurements, mildly functionalized MoS$_2$ such as NH$_2$Ph-MoS$_2$, OMePh-MoS$_2$, ProPh-MoS$_2$, and Ph-MoS$_2$ with the degree of functionalization in the range of L:MoS$_2 \leq$ 0.2 displays better thermal stability compared to heavily functionalized MoS$_2$ (L:MoS$_2 > 0.2$) such as NO$_2$Ph-MoS$_2$ and COOHPh-MoS$_2$, as well as *ce*-MoS$_2$ (Figure 3 and S2). The mild modification (L:MoS$_2 \leq 0.2$) likely heals the SVs, resulting in a more robust crystal structure of MoS$_2$, while the heavy modification (L:MoS$_2 > 0.2$) introduces local strain,[49–54] which might weaken the intralayer bonds of MoS$_2$, rendering a relatively vulnerable structure and thus possibly more exposed edges. The change of grain size,[55–57] caused by the high degree of functionalization when L:MoS$_2 > 0.2$, potentially accounts for the different scaling of the Raman intensity ratio across this
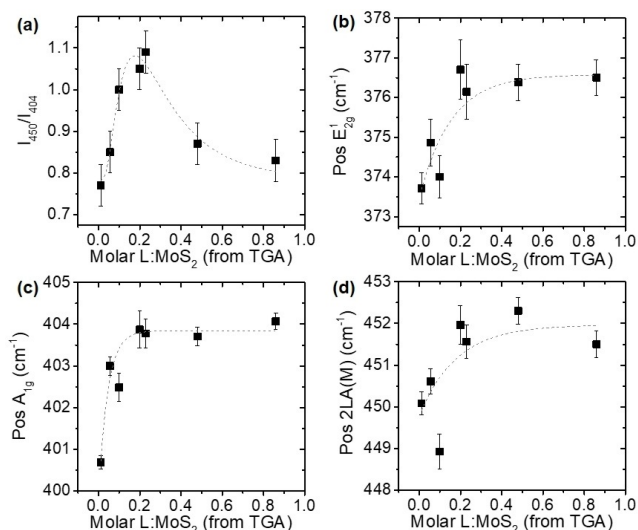
Chemistry–A European Journal

Full Paper
doi.org/10.1002/chem.202000286

**Chemistry
Europe**
European Chemical
Societies Publishing

Figure 7. (a) Plot of the intensity of the 2LA(M) peak normalized to the A_{1g} peak (I_{450}/I_{404}) as a function of the degree of functionalization. (b–d) Plots of the peak position of E^1_{2g}, A_{1g}, and 2LA (M) as a function of the degree of functionalization. The dashed lines are guides for the eye.

point. In other words, without disturbing the integrity of MoS_2 nanosheets, the maximum sulfur vacancy modification can be achieved when about 20% of surface addends are introduced. Interestingly, this two-regime feature of I_{450}/I_{404} with the change of defect density in MoS_2 resembles qualitatively the relationship of I_D/I_G vs. L_D (interdefect distance) in graphene-based system.[58] Accordingly, we suggest that the intensity ratio of 2LA(M) to A_{1g} can be used as an indicator to quantify the defect density and monitor the effectiveness of the defect engineering process in the MoS_2-based system.

In addition, we observe other (minor) changes in the peak intensity ratios of the other main Raman modes as illustrated by the plots of the intensity of the 2LA(M) peak normalized to the E^1_{2g} peak (I_{450}/I_{377}) as well as the intensity of the E^1_{2g} peak normalized to the A_{1g} peak (I_{377}/I_{404}) as a function of the degree of functionalization (Figure S6). I_{450}/I_{377} and I_{377}/I_{404} undergo a monotonous change with the increase of the degree of functionalization. Specifically, I_{377}/I_{404} decreases linearly with increasing defect functionalization (with a slope of −0.26), while I_{450}/I_{377} increases (with a slope of +0.27). A detailed Raman study and theoretical calculations would be helpful to provide more insights into how and why SV modification affects these Raman intensity ratios, however, this is beyond the scope of this manuscript.

To further investigate the influence of SV modification on the Raman scattering of MoS_2, we analyzed the shift of the characteristic Raman modes with the change of the degree of functionalization. To better identify the shift in peak position of different Raman modes, we deconvoluted the main Raman peaks by fitting the data to four Lorentzians (Figure S7). The fitted red, green, blue and pink lines correspond to the E^1_{2g}, A_{1g}, B_{1u}, and 2LA(M) modes, respectively. In Figure 7b, c, and d, we plot the Raman shift of E^1_{2g}, A_{1g}, and 2LA (M) as a function of the degree of functionalization. The trend of A_{1g}, E^1_{2g} and

2LA (M) peak position shift is indicated by the grey dashed line. With increasing the degree of functionalization (decrease of SV density), the peak positions of the E^1_{2g} (Pos E^1_{2g}), A_{1g} (Pos A_{1g}), and 2LA(M) (Pos 2LA(M)) modes gradually shift to higher frequency before plateauing at $L:MoS_2 \approx 0.2$. When the degree of functionalization is below the critical point ($L:MoS_2 = 0.2$), the stiffening of E^1_{2g}, A_{1g}, and 2LA (M) scales with the degree of functionalization. The saturation of the peak shift at $L:MoS_2 > 0.2$ implies again that a degree of functionalization of around 20% is a critical point for the defect engineering process.

Defect engineering of MoS_2 using thiophenols results in the formation of a functionalized surface which is characterized by healed SVs and covalently tethered functional groups. Previous studies by other groups have shown that a variation in defect concentration and surface addends can introduce local strains and doping effects, which would significantly affect the Raman frequencies.[49, 50] Therefore, we tentatively attribute the upshift of A_{1g}, E^1_{2g}, and 2LA(M) modes in defect-engineered MoS_2 samples to the variation of local strains as well as doping effects even though other factors such as variations in 1T/2H content can also play a role.[59]

The doping effect associated with defect engineering was also verified by the extinction spectra of modified MoS_2 samples (Figure 8a). Compared to the extinction spectrum of ce-MoS_2 (grey curve in Figure 8a), the defect-engineered MoS_2 samples display an intensified peak (peak A) between 300–400 nm. This peak can be more clearly distinguished in the second derivative spectra (Figure S8a). Figure 8b shows a plot of the peak position (Pos A) determined from the second derivative spectra as a function of the Hammett parameter of the functional groups. We observe a peak around a Hammett parameter of 0.3 (BrPh-). The extinction of the peak A is red-shifted for samples with a larger absolute value of the Hammett parameter (e.g. NO_2Ph- and NH_2Ph-). The correlation between the magnitude of the peak shift and the strength of the elec-
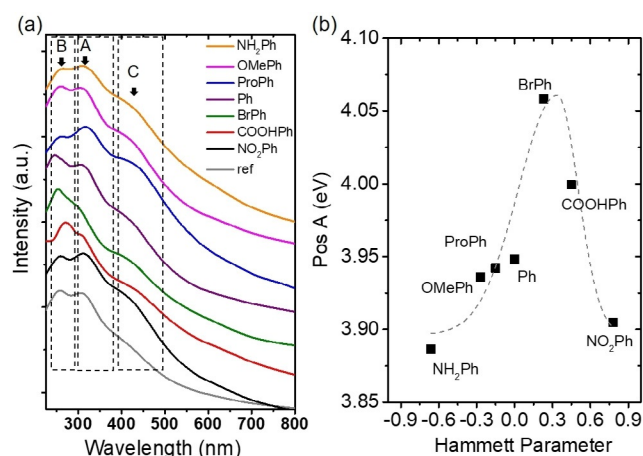

Figure 8. (a) Extinction spectra of ce-MoS_2 and defect-engineered MoS_2 dispersions. Spectra are offset for clarity. (b) Plot of the position of peak A (≈ 320 nm) in the defect-engineered MoS_2 as a function of the Hammett parameter. The dashed line is a guide for the eye.

Chemistry–A European Journal

Full Paper
doi.org/10.1002/chem.202000286

Chemistry Europe
European Chemical
Societies Publishing

tron density change on the phenyl ring strongly suggests that the shift is related to the doping of MoS_2.

We note that for Ph-MoS_2 and COOHPh-MoS_2, the position of peak A is a bit more red-shifted than expected from the envelope curve, which we attribute to the pronounced aggregation observed in these two samples. As discussed above, Ph-MoS_2 and COOHPh-MoS_2 show the most significant zeta potential drop relative to ce-MoS_2, indicating the worst colloidal stability among all modified samples. This results in a stronger contribution from light scattering to the optical extinction spectra. Since the scattering spectrum of MoS_2 in the resonant regime was reported to follow the absorbance in shape, albeit with a red-shift,[60] the observed behavior is fully consistent with aggregation. The plot of the position of peak B at 250 nm in all modified MoS_2 samples against their zeta potentials (Figure S8b) further demonstrates that the increase of scattering in poorly dispersed samples would lead to a red shift of the extinction spectral profile. Furthermore, we note that all the modified MoS_2 samples show an intensified extinction band (peak C) at around 450 nm in the visible region. This spectral region coincides with the dominant absorbance of 2H-MoS_2 (around the C-exciton),[61] suggesting the partial restoration of the 2H-phase after the defect engineering process. This is potentially related to the stability of the two polytypes: 2H-MoS_2 is thermodynamically more stable than 1T or 1T'-MoS_2[1,52] and thus phase transition from 1T to 2H is favorable even under ambient conditions. Similar phenomena have been reported in other covalently functionalized MoS_2 systems.[62]

Conclusions

We demonstrated an approach to controllably engineer the SVs of chemically exfoliated MoS_2 nanosheets using a series of thiophenol derivatives in solution. The degree of functionalization associated with the density of SVs in MoS_2 can be systematically tuned by adjusting the functional groups in thiophenols. We observed a phenomenological relationship between the intensity of 2LA(M) mode relative to A_{1g} mode and the degree of functionalization, which can potentially serve as a spectroscopic indicator to monitor and quantify the defect engineering process. We believe our method of controlled defect functionalization of MoS_2 in solution can encourage further exploration of practical strategies to fulfill scalable production and application of defect-free MoS_2 in a broad range.

Experimental Section

Materials

MoS_2 powder was purchased from Sigma Aldrich and dried at 80 °C overnight under vacuum before use. n-butyllithium (2.0 M) in cyclohexane, n-hexane (anhydrous, 95 %), cyclohexane, ethanol, isopropanol, thiophenol, toluene, 4-bromothiophenol (95 %), 4-isopropylthiophenol (95 %), p-nitrothiophenol (80 %), mercaptoanisol (97 %), 4-mercaptobenzoic acid (90 %), and 4-aminothiophenol (97 %) were purchased from Sigma Aldrich and used as received.

Preparation of chemically exfoliated MoS_2 nanosheets (ce-MoS_2)

Inside a glovebox (< 0.1 ppm O_2, < 0.1 ppm H_2O), 300 mg pre-dried MoS_2 powder was added to n-butyllithium (2.0 M in cyclohexane, 3 mL) and the mixture was stirred at room temperature for 2 days. Then the reaction mixture was taken out of the glovebox and diluted with anhydrous n-hexane (10 mL). Subsequently, the diluted reaction mixture was added dropwise to de-ionized water (200 mL) at 0 °C to form a black slurry. After the gas generation ceased, the organic impurities in this black slurry were removed by extraction with cyclohexane (200 mL) and the aqueous phase was collected in a Duran® bottle and deaerated under Argon flow for 15 min. The resulting aqueous dispersion was sealed and subjected to bath-sonication (Bandelin, Sonorex DigiPlus, DL 255 H, 35 kHz) at room temperature for 1 h and then subjected to centrifugation at 750 rpm (630 g, Sigma 3–30 K centrifuge equipped with a fixed angle rotor 12159) at 15 °C for 1 h to remove the heavier non-exfoliated MoS_2 in the sediment. The exfoliated material in the supernatant was collected and thoroughly washed with de-ionized water through three times of high-speed centrifugation at 13000 rpm (189280 g, 1 h, 15 °C) to remove very small flakes of MoS_2 and LiOH in the supernatant. The sediment after all washing steps was re-dispersed in de-ionized water for further functionalization and characterization.

General procedure for functionalization of ce-MoS_2 with thiophenols

The aqueous dispersion of ce-MoS_2 (0.5–1.0 mg mL^{-1}, 50 mL) was mixed with 20 molar excess of thiophenol derivatives dispersed in isopropanol (25 mL) in a Schlenk flask. The mixture was subjected to freeze-pump-thaw cycling for three times to remove all the air in dispersion and then vigorously stirred at 50 °C for 48 h under Ar. The resulting reaction mixture was purified through washing with ethanol, isopropanol, and de-ionized water. The purified materials were re-dispersed in water or isopropanol for further characterization.

Reference experiment: preparation of ce-MoS_2/toluene mixture

Absolute toluene was mixed with ethanol (40 mL, v/v = 1/1). Then the organic solution was added to ce-MoS_2 aqueous dispersion (0.5–1.0 mg mL^{-1}, 80 mL) and stirred at 50 °C for 48 h under Ar. The resulting reaction mixture was purified through washing with ethanol, isopropanol, and de-ionized water. The purified materials were re-dispersed in isopropanol for further characterization.

Characterization and instrumentation

Atomic force microscopy (AFM) was carried out using a Bruker Dimension Icon microscope. The MoS_2 samples were prepared by spin coating a solution of a given sample at 3000 rpm on Si/SiO$_2$ wafers (300 nm). Bruker Scanasyst-Air silicon tips on nitride levers with a spring constant of 0.4 N m^{-1} were used to obtain images resolved by 5120×512 or 1024×1024 pixels. For thermogravimetric analysis coupled with mass spectrometry (TGA-MS), the dispersion of an individual sample was filtered through a cellulose membrane (0.2 μm, Sartorius). The material was then collected and dried under vacuum overnight before subjected to the further analysis. TGA-MS measurements were carried out on a Netzsch STA 409 CD instrument equipped with a Skimmer QMS 422 mass spectrometer (MS/EI) with the following programmed time-dependent tempera-

Chemistry–A European Journal

Full Paper
doi.org/10.1002/chem.202000286

Chemistry Europe
European Chemical
Societies Publishing

ture profile: 30–700 °C with 10 K min⁻¹ gradient. The initial sample weights were about 3–5 mg, and the experiments were performed under inert gas atmosphere with a Helium gas flow of 80 mL min⁻¹. Raman spectroscopy was recorded on Horiba Jobin Yvon LabRAM Aramis confocal Raman microscope with a 633 nm excitation laser (size of laser spot ≈1 μm) in air under ambient conditions. The Raman emission was collected by a 50 Å objective (Olympus LMPlanF1 50×LWD, NA 0.5) and dispersed by 600 lines mm⁻¹ grating. The spectrometer was calibrated in frequency using a standard silicon wafer. The mean spectrum of 121 measured Raman single point spectra from a 100 μm² map is displayed. For X-ray photoelectron spectroscopy (XPS) measurements, the samples were prepared by placing the pre-dried sample powder onto the Scotch crystal tape. Here, a PHI VersaProbe III instrument equipped with a micro-focused monochromated Al$_{Kα}$ source (1486.6 eV) and dual beam charge neutralization was used. Core level spectra were recorded with PHI SmartSoft VersaProbe software and processed with PHI MultiPak 9.8. Sputter depth profiling was conducted using 1 KeV Ar⁺ ions. Binding energies were referenced to the adventitious carbon signal at 284.8 eV. After subtraction of a Shirley type background, the spectra were fitted with Gaussian-Lorentzian peak shapes. High resolution transmission electron microscopy (TEM) analysis was performed on a state-of-the-art double corrected Titan Themis³ 300 operated at 300 kV. The adjusted special aberration coefficient was Cs = −10 μm. All images were acquired by a FEI 4k Ceta CMOS camera. All the TEM samples were prepared via drop casting MoS₂ samples in isopropanol on the common copper TEM grids. Before drop casting, a purification step with a high-speed centrifugation was performed. Afterwards, most of the solvent was exchanged with clean isopropanol. The TEM grids were also cleaned with isopropanol before the preparation. The post-treatment of the samples was an ethanol bath of the whole TEM grid for 5 min to remove suspicious surface contaminants. All prepared samples were dried under vacuum overnight. For Fourier-transform infrared spectroscopy (FT-IR), the spectra were recorded on a Bruker Tensor 27 (ATR plate) spectrometer (Billerica, MA, USA), or IR Prestige-21 spectrometer (ATR plate) (Shimadzu, Japan). All the samples were prepared by vacuum filtration of respective dispersion onto the cellulose membrane (0.2 μm, Sartorius), collected and dried under vacuum overnight. For nuclear magnetic resonance spectroscopy (NMR), ¹H NMR spectra were recorded on Bruker Avance 400 (400 MHz) and Jeol EX 400 (400 MHz) spectrometers. Thiophenol (20 μL) was dissolved in CD₃OD (3 mL) as a reference for the ¹H NMR measurement. The purified Ph-MoS₂ (≈0.4 mg) was re-dispersed in CD₃OD (3 mL) with the aid of mild sonication in bath for 5 min and subjected to the NMR measurement. UV/Vis spectra were recorded on a Shimadzu UV-3102 PC UV/Vis NIR scanning spectrophotometer in quartz cuvettes. The aqueous dispersion of ce-MoS₂ was diluted by 50 folds and then subjected to the measurement. The functionalized materials were dispersed in isopropanol for the UV/Vis measurement. Zeta potential (ζ) measurements were performed on a Malvern Zetasizer Nano system ZEN3600 with irradiation from a 633 nm He-Ne laser. The samples were injected in folded capillary cells (DTS1070), and the electrophoretic mobility (μ) was measured using a combination of electrophoresis and laser Doppler velocimetry techniques. The zeta potential ζ is related to the measured electrophoretic mobility μ according to the Smoluchowski approximation. The mean of 5 measurements is displayed. All measurements were recorded at 25 °C.

Conflict of interest

The authors declare no conflict of interest.

[1] M. Chhowalla, H. S. Shin, G. Eda, L.-J. Li, K. P. Loh, H. Zhang, *Nat. Chem.* **2013**, *5*, 263–275.
[2] B. Radisavljevic, A. Radenovic, J. Brivio, V. Giacometti, A. Kis, *Nat. Nanotechnol.* **2011**, *6*, 147–150.
[3] X. Zhang, Z. Lai, Q. Ma, H. Zhang, *Chem. Soc. Rev.* **2018**, *47*, 3301–3338.
[4] S. Manzeli, D. Ovchinnikov, D. Pasquier, O. V. Yazyev, A. Kis, *Nat. Rev. Mater.* **2017**, *2*, 17033.
[5] M. Amani, D.-H. Lien, D. Kiriya, J. Xiao, A. Azcatl, J. Noh, S. R. Madhvapathy, R. Addou, S. KC, M. Dubey, K. Cho, R. M. Wallace, S.-C. Lee, J.-H. He, J. W. Ager, X. Zhang, E. Yablonovitch, A. Javey, *Science* **2015**, *350*, 1065–1068.
[6] M. Samadi, N. Sarikhani, M. Zirak, H. Zhang, H.-L. Zhang, A. Z. Moshfegh, *Nanoscale Horiz.* **2018**, *3*, 90–204.
[7] G. Eda, H. Yamaguchi, D. Voiry, T. Fujita, M. Chen, M. Chhowalla, *Nano Lett.* **2011**, *11*, 5111–5116.
[8] K. S. Novoselov, D. Jiang, F. Schedin, T. J. Booth, V. V. Khotkevich, S. V. Morozov, A. K. Geim, *Proc. Natl. Acad. Sci. USA* **2005**, *102*, 10451–10453.
[9] Y.-H. Lee, X.-Q. Zhang, W. Zhang, M.-T. Chang, C.-T. Lin, K.-D. Chang, Y.-C. Yu, J. T.-W. Wang, C.-S. Chang, L.-J. Li, T.-W. Lin, *Adv. Mater.* **2012**, *24*, 2320–2325.
[10] J. N. Coleman, M. Lotya, A. O'Neill, S. D. Bergin, P. J. King, U. Khan, K. Young, A. Gaucher, S. De, R. J. Smith, I. V. Shvets, S. K. Arora, G. Stanton, H.-Y. Kim, K. Lee, G. T. Kim, G. S. Duesberg, T. Hallam, J. J. Boland, J. J. Wang, J. F. Donegan, J. C. Grunlan, G. Moriarty, A. Shmeliov, R. J. Nicholls, J. M. Perkins, E. M. Grieveson, K. Theuwissen, D. W. McComb, P. D. Nellist, V. Nicolosi, *Science* **2011**, *331*, 568–571.
[11] P. Joensen, R. F. Frindt, S. R. Morrison, *Mater. Res. Bull.* **1986**, *21*, 457–461.
[12] H. Wang, Z. Lu, S. Xu, D. Kong, J. J. Cha, G. Zheng, P.-C. Hsu, K. Yan, D. Bradshaw, F. B. Prinz, Y. Cui, *Proc. Natl. Acad. Sci. USA* **2013**, *110*, 19701–19706.
[13] Y. Yu, G.-H. Nam, Q. He, X.-J. Wu, K. Zhang, Z. Yang, J. Chen, Q. Ma, M. Zhao, Z. Liu, F.-R. Ran, X. Wang, H. Li, X. Huang, B. Li, Q. Xiong, Q. Zhang, Z. Liu, L. Gu, Y. Du, W. Huang, H. Zhang, *Nat. Chem.* **2018**, *10*, 638–643.
[14] J. Zheng, H. Zhang, S. Dong, Y. Liu, C. Tai Nai, H. Suk Shin, H. Young Jeong, B. Liu, K. Ping Loh, *Nat. Commun.* **2014**, *5*, 2995.
[15] C. Backes, T. M. Higgins, A. Kelly, C. Boland, A. Harvey, D. Hanlon, J. N. Coleman, *Chem. Mater.* **2017**, *29*, 243–255.
[16] W. Zhou, X. Zou, S. Najmaei, Z. Liu, Y. Shi, J. Kong, J. Lou, P. M. Ajayan, B. I. Yakobson, J.-C. Idrobo, *Nano Lett.* **2013**, *13*, 2615–2622.
[17] Y.-C. Lin, T. Björkman, H.-P. Komsa, P.-Y. Teng, C.-H. Yeh, F.-S. Huang, K.-H. Lin, J. Jadczak, Y.-S. Huang, P.-W. Chiu, A. V. Krasheninnikov, K. Suenaga, *Nat. Commun.* **2015**, *6*, 6736.
[18] H.-P. Komsa, S. Kurasch, O. Lehtinen, U. Kaiser, A. V. Krasheninnikov, *Phys. Rev. B* **2013**, *88*, 035301.

Chemistry–A European Journal

Full Paper
doi.org/10.1002/chem.202000286

Chemistry Europe
European Chemical
Societies Publishing

[19] A. M. van der Zande, P. Y. Huang, D. A. Chenet, T. C. Berkelbach, Y. You, G.-H. Lee, T. F. Heinz, D. R. Reichman, D. A. Muller, J. C. Hone, *Nat. Mater.* **2013**, *12*, 554.

[20] S. Roy, W. Choi, S. Jeon, D.-H. Kim, H. Kim, S. J. Yun, Y. Lee, J. Lee, Y.-M. Kim, J. Kim, *Nano Lett.* **2018**, *18*, 4523–4530.

[21] R. Addou, L. Colombo, R. M. Wallace, *ACS Appl. Mater. Interfaces* **2015**, *7*, 11921–11929.

[22] Z. Lin, B. R. Carvalho, E. Kahn, R. Lv, R. Rao, H. Terrones, M. A. Pimenta, M. Terrones, *2D Mater.* **2016**, *3*, 022002.

[23] D.-H. Lien, S. Z. Uddin, M. Yeh, M. Amani, H. Kim, J. W. Ager, E. Yablonovitch, A. Javey, *Science* **2019**, *364*, 468–471.

[24] S. S. Chou, M. De, J. Kim, S. Byun, C. Dykstra, J. Yu, J. Huang, V. P. Dravid, *J. Am. Chem. Soc.* **2013**, *135*, 4584–4587.

[25] H. Li, C. Tsai, A. L. Koh, L. Cai, A. W. Contryman, A. H. Fragapane, J. Zhao, H. S. Han, H. C. Manoharan, F. Abild-Pedersen, J. K. Nørskov, X. Zheng, *Nat. Mater.* **2016**, *15*, 48.

[26] X. Chen, A. R. McDonald, *Adv. Mater.* **2016**, *28*, 5738–5746.

[27] S. Bertolazzi, M. Gobbi, Y. Zhao, C. Backes, P. Samorì, *Chem. Soc. Rev.* **2018**, *47*, 6845–6888.

[28] E. P. Nguyen, B. J. Carey, J. Z. Ou, J. van Embden, E. D. Gaspera, A. F. Chrimes, M. J. S. Spencer, S. Zhuiykov, K. Kalantar-zadeh, T. Daeneke, *Adv. Mater.* **2015**, *27*, 6225–6229.

[29] X. Chen, N. C. Berner, C. Backes, G. S. Duesberg, A. R. McDonald, *Angew. Chem. Int. Ed.* **2016**, *55*, 5803–5808; *Angew. Chem.* **2016**, *128*, 5897–5902.

[30] X. Chen, C. McGlynn, A. R. McDonald, *Chem. Mater.* **2018**, *30*, 6978–6982.

[31] A. Förster, S. Gemming, G. Seifert, D. Tománek, *ACS Nano* **2017**, *11*, 9989–9996.

[32] J. Martincová, M. Otyepka, P. Lazar, *Chem. Eur. J.* **2017**, *23*, 13233–13239.

[33] R. C. Longo, R. Addou, S. Kc, J.-Y. Noh, C. M. Smyth, D. Barrera, C. Zhang, J. W. P. Hsu, R. M. Wallace, K. Cho, *2D Mater.* **2017**, *4*, 025050.

[34] J. Pető, T. Ollár, P. Vancsó, Z. I. Popov, G. Z. Magda, G. Dobrik, C. Hwang, P. B. Sorokin, L. Tapasztó, *Nat. Chem.* **2018**, *10*, 1246–1251.

[35] D. M. Sim, M. Kim, S. Yim, M.-J. Choi, J. Choi, S. Yoo, Y. S. Jung, *ACS Nano* **2015**, *9*, 12115–12123.

[36] Q. Li, Y. Zhao, C. Ling, S. Yuan, Q. Chen, J. Wang, *Angew. Chem. Int. Ed.* **2017**, *56*, 10501–10505; *Angew. Chem.* **2017**, *129*, 10637–10641.

[37] Q. Ding, K. J. Czech, Y. Zhao, J. Zhai, R. J. Hamers, J. C. Wright, S. Jin, *ACS Appl. Mater. Interfaces* **2017**, *9*, 12734–12742.

[38] Z. Yu, Y. Pan, Y. Shen, Z. Wang, Z.-Y. Ong, T. Xu, R. Xin, L. Pan, B. Wang, L. Sun, J. Wang, G. Zhang, Y. W. Zhang, Y. Shi, X. Wang, *Nat. Commun.* **2014**, *5*, 5290.

[39] M. Makarova, Y. Okawa, M. Aono, *J. Phys. Chem. C* **2012**, *116*, 22411–22416.

[40] K. C. Knirsch, N. C. Berner, H. C. Nerl, C. S. Cucinotta, Z. Gholamvand, N. McEvoy, Z. Wang, I. Abramovic, P. Vecera, M. Halik, S. Sanvito, G. S. Duesberg, V. Nicolosi, F. Hauke, A. Hirsch, J. N. Coleman, C. Backes, *ACS Nano* **2015**, *9*, 6018–6030.

[41] D. Voiry, M. Salehi, R. Silva, T. Fujita, M. Chen, T. Asefa, V. B. Shenoy, G. Eda, M. Chhowalla, *Nano Lett.* **2013**, *13*, 6222–6227.

[42] D. Voiry, A. Goswami, R. Kappera, C. de Carvalho Castro e Silva, D. Kaplan, T. Fujita, M. Chen, T. Asefa, M. Chhowalla, *Nat. Chem.* **2015**, *7*, 45–49.

[43] G. Eda, T. Fujita, H. Yamaguchi, D. Voiry, M. Chen, M. Chhowalla, *ACS Nano* **2012**, *6*, 7311–7317.

[44] P. Cheng, K. Sun, Y. H. Hu, *RSC Adv.* **2016**, *6*, 65691–65697.

[45] K. Gołasa, M. Grzeszczyk, R. Bożek, P. Leszczyński, A. Wysmołek, A. Babiński, *Solid State Commun.* **2014**, *197*, 53–56.

[46] S. Jiménez Sandoval, D. Yang, R. F. Frindt, J. C. Irwin, *Phys. Rev. B* **1991**, *44*, 3955–3962.

[47] M. Calandra, *Phys. Rev. B* **2013**, *88*, 245428.

[48] A. Molina-Sánchez, L. Wirtz, *Phys. Rev. B* **2011**, *84*, 155413.

[49] S. Mignuzzi, A. J. Pollard, N. Bonini, B. Brennan, I. S. Gilmore, M. A. Pimenta, D. Richards, D. Roy, *Phys. Rev. B* **2015**, *91*, 195411.

[50] Q. Qian, Z. Zhang, K. J. Chen, *Langmuir* **2018**, *34*, 2882–2889.

[51] L. Yang, X. Cui, J. Zhang, K. Wang, M. Shen, S. Zeng, S. A. Dayeh, L. Feng, B. Xiang, *Sci. Rep.* **2014**, *4*, 5649.

[52] Y. Wang, C. Cong, C. Qiu, T. Yu, *Small* **2013**, *9*, 2857–2861.

[53] C. Rice, R. J. Young, R. Zan, U. Bangert, D. Wolverson, T. Georgiou, R. Jalil, K. S. Novoselov, *Phys. Rev. B* **2013**, *87*, 081307.

[54] A. Castellanos-Gomez, R. Roldán, E. Cappelluti, M. Buscema, F. Guinea, H. S. J. van der Zant, G. A. Steele, *Nano Lett.* **2013**, *13*, 5361–5366.

[55] É. Blanco, P. Afanasiev, G. Berhault, D. Uzio, S. Loridant, *C. R. Chim.* **2016**, *19*, 1310–1314.

[56] T.-X. Huang, X. Cong, S.-S. Wu, K.-Q. Lin, X. Yao, Y.-H. He, J.-B. Wu, Y.-F. Bao, S.-C. Huang, X. Wang, P.-H. Tan, B. Ren, *Nat. Commun.* **2019**, *10*, 5544.

[57] Y. Guo, W. Zhang, H. Wu, J. Han, Y. Zhang, S. Lin, C. Liu, K. Xu, J. Qiao, W. Ji, Q. Chen, S. Gao, W. Zhang, X. Zhang, Y. Chai, *Sci. Adv.* **2018**, *4*, 6252.

[58] L. G. Cançado, A. Jorio, E. H. M. Ferreira, F. Stavale, C. A. Achete, R. B. Capaz, M. V. O. Moutinho, A. Lombardo, T. S. Kulmala, A. C. Ferrari, *Nano Lett.* **2011**, *11*, 3190–3196.

[59] S. J. R. Tan, I. Abdelwahab, Z. Ding, X. Zhao, T. Yang, G. Z. J. Loke, H. Lin, I. Verzhbitskiy, S. M. Poh, H. Xu, C. T. Nai, W. Zhou, G. Eda, B. Jia, K. P. Loh, *J. Am. Chem. Soc.* **2017**, *139*, 2504–2511.

[60] C. Backes, R. J. Smith, N. McEvoy, N. C. Berner, D. McCloskey, H. C. Nerl, A. O'Neill, P. J. King, T. Higgins, D. Hanlon, N. Scheuschner, J. Maultzsch, L. Houben, G. S. Duesberg, J. F. Donegan, V. Nicolosi, J. N. Coleman, *Nat. Commun.* **2014**, *5*, 4576.

[61] J. A. Wilson, A. D. Yoffe, *Adv. Phys.* **1969**, *18*, 193–335.

[62] X. Chen, D. McAteer, C. McGuinness, I. Godwin, J. N. Coleman, A. R. McDonald, *Chem. Eur. J.* **2018**, *24*, 351–355.